ELSEVIER

International Journal of Heat and Fluid Flow 22 (2001) 259–271

International Journal of HEAT AND FLUID FLOW

www.elsevier.com/locate/ijhff

Application of a three-equation cubic eddy viscosity model to 3-D turbulent flows by the unstructured grid method

K. Suga [a,*], M. Nagaoka [a], N. Horinouchi [a], K. Abe [a,b], Y. Kondo [a]

[a] *Heat Transfer Lab., Toyota Central R&D Labs. Inc., Nagakute, Aichi 480-1192, Japan*
[b] *Department of Aeronautics and Astronautics, Kyushu University, Fukuoka 812-8581, Japan*

Abstract

The three-equation cubic k–ε–A_2 model proposed by Craft et al. (Int. J. Heat Fluid Flow 18 (1997) 15–28) is evaluated in three-dimensional (3-D) turbulent flows pertinent to engineering applications, especially in the automobile industry. For the computations of complex industrial flows, a numerical scheme has been developed using the cell vertex unstructured grid method. This scheme treats a mixture of tetrahedral, pyramidal, prismatic and hexahedral computational cells with high accuracy. The industrial flows chosen are internal combustion (IC) engine port-cylinder flows and flows around aerodynamic bluff bodies. The model performance in U-bend duct flows and a flow around a surface-mounted cubical obstacle is also examined. These fundamental flows include essential features of the industrial flows presently focused on. The model performs generally satisfactorily. However, the performance in a 3-D separating wake flow behind a bluff body suggests that the model needs further improvements.

Keywords: Nonlinear eddy viscosity model; Unstructured grid method; 3-D industrial turbulent flows; U-bend duct flows; IC engine flows; Aerodynamic flows

1. Introduction

Since a variety of software packages for computational fluid dynamics (CFD) have been commercialized, CFD is now recognized as an essential tool for industrial engineers. In industrial CFD applications, an eddy viscosity model (EVM) is widely applied to account for turbulence. This is especially true in three-dimensional (3-D) flow computations because its computational requirements are reasonable in terms of costs and memories.

However, the validation of the standard linear EVMs, is now well established and many anomalies corresponding to the linear stress–strain relation are recognized. The typical shortcomings are found in stagnation flows, swirling flows, flows driven by turbulence and flows near curved boundaries. In order to remove some of these with a reasonable extra load, the use of a nonlinear stress–strain relation has been focused on, particularly in the last decade (e.g. Myong and Kasagi, 1990; Rubinstein and Barton, 1990; Gatski and Speziale, 1993; Shih et al., 1995). Most of them are quadratic EVMs and many of the low Reynolds number versions, however, still employ a parameter of wall distance for introducing near wall effects (e.g. Myong and Kasagi, 1990; Abe et al., 1997). Such a topographical parameter is hard to be defined in complicated flow fields and thus undesirable to be used in the model expressions.

Since it is one of the rare models totally free from the topographical parameters, the k–ε–A_2 cubic EVM of Craft et al. (1997) may be suitable for complicated industrial flows though it requires to solve the third transport equation for A_2 which is the second invariant of the anisotropic Reynolds stress tensor. Moreover, the cubic EVM is promising in industrial flows, since the cubic terms have sensitivity to streamline curvature (Suga, 1995; Craft et al., 1996) which is essential in most 3-D flow fields. In fact, the k–ε–A_2 model showed many encouraging validation results (Craft et al., 1997; Chen et al., 1998a,b; Barakos and Drikakis, 2000). However, all of the flows tested were essentially 2-D. Therefore, the present study focuses on the model validation in 3-D industrial flows pertinent to the automobile engineering.

In designing the intake-port of an internal combustion (IC) engine, its curvature ratio is one of the important parameters. It is a factor to determine the total engine height and significantly affects the gas discharge rate. In a strong curvature case, a separation bubble appears along the suction side of the port and effectively blocks the flow so that the gas discharge into the cylinder reduces. Thus, curved duct flows (U-bend flows) of Chang et al. (1983) and Cheah et al. (1994) are considered as fundamental test cases prior to computations of the IC engine port-cylinder flows of Kawazoe (1993).

As for the aerodynamic design of an automobile, one of the crucial parameters for the drag performance is the slant angle

* Corresponding author.
E-mail address: suga@flow.tytlabs.co.jp (K. Suga).

0142-727X/01/$ - see front matter
PII: S0142-727X(01)00088-1

Notation

a_{ij}	anisotropic stress ($\equiv \overline{u_i u_j}/k - 2/3\delta_{ij}$)
A	stress flatness parameter [$\equiv 1 - \frac{9}{8}(a_{ij}a_{ij} - a_{ij}a_{jk}a_{ki})$]
A_2, A_3	the second and the third invariants of anisotropic stress ($\equiv a_{ij}a_{ij}, a_{ij}a_{jk}a_{ki}$)
C_D	drag coefficient
C_f	discharge coefficient
D	duct height or port diameter
H	bluff body or obstacle height
k	turbulence energy
l	turbulent length scale ($\equiv k^{1.5}/\varepsilon$)
R, Rc	port and duct bend radii
Re	bulk Reynolds number
$\tilde{R}_t$	turbulent Reynolds number [$\equiv k^2/(\nu\tilde{\varepsilon})$]
$S_{ij}, \tilde{S}$	$\equiv (\partial U_i/\partial x_j) + (\partial U_j/\partial x_i)$, $\tau\sqrt{S_{ij}S_{ij}/2}$
u_i, U_i	fluctuating and mean velocity components
$\overline{u_i u_j}$	Reynolds stress
U_b, U_c	bulk and centre-line velocities
x_i	coordinate direction
γ	specific heat ratio
δ_{ij}	Kronecker's delta
$\varepsilon, \tilde{\varepsilon}$	dissipation rate of k, $\varepsilon - 2\nu(\partial\sqrt{k}/\partial x_k)(\partial\sqrt{k}/\partial x_k)$
ν, ν_t	kinematic viscosity, kinematic eddy viscosity
ξ, η, ζ	local coordinate directions
ρ	fluid density
τ	turbulent time scale ($\equiv k/\tilde{\varepsilon}$)
ϕ	variable
$\Omega_{ij}, \tilde{\Omega}$	$\equiv (\partial U_i/\partial x_j) - (\partial U_j/\partial x_i)$, $\tau\sqrt{\Omega_{ij}\Omega_{ij}/2}$

of the back window (Ahmed et al., 1984). Due to the size of the flow separation induced by the slant, the drag coefficient changes significantly. Hence, flows around bluff bodies with a slant back of Maeda et al. (1990) are selected for the validation. Since predicting 3-D separating wake flows is important for such a flow computation, a flow around a cubical obstacle (Martinuzzi et al., 1993) is also considered as a further test case.

For the computations of these complex 3-D flows, a CFD code is newly developed in the present study using the cell vertex collocated unstructured grid method. This code works on a mixture of tetrahedral, pyramidal, prismatic and hexahedral computational cells with high accuracy. Thus, this paper also describes some new aspects of the discretization method on unstructured grids.

2. Turbulence model

In the eddy viscosity modelling, the stress–strain relation may be written as

$$\overline{u_i u_j} = \frac{2}{3}\delta_{ij}k - \nu_t S_{ij} + \mathrm{Hot}_{ij}, \tag{1}$$

where $\nu_t (= c_\mu k^2/\tilde{\varepsilon})$ is the kinematic eddy viscosity and Hot_{ij} is the higher-order term comprising the products of S_{ij} and Ω_{ij}. The k–ε–A_2 cubic EVM of Craft et al. (1997) introduces up to the cubic-order terms, and thus Hot_{ij} may be written in the following form:

$$\begin{aligned}\mathrm{Hot}_{ij} = {} & c_1\nu_t\tau(S_{ik}S_{kj} - \tfrac{1}{3}S_{kl}S_{kl}\delta_{ij}) + c_2\nu_t\tau(\Omega_{ik}S_{kj} + \Omega_{jk}S_{ki}) \\ & + c_3\nu_t\tau(\Omega_{ik}\Omega_{jk} - \tfrac{1}{3}\Omega_{lk}\Omega_{lk}\delta_{ij}) + c_4\nu_t\tau^2(S_{ki}\Omega_{lj} + S_{kj}\Omega_{li})S_{kl} \\ & + c_5\nu_t\tau^2(\Omega_{il}\Omega_{lm}S_{mj} + S_{il}\Omega_{lm}\Omega_{mj} - \tfrac{2}{3}S_{lm}\Omega_{mn}\Omega_{nl}\delta_{ij}) \\ & + c_6\nu_t\tau^2 S_{ij}S_{kl}S_{kl} + c_7\nu_t\tau^2 S_{ij}\Omega_{kl}\Omega_{kl}.\end{aligned} \tag{2}$$

As shown in Table 1, the model coefficients include the dependency of A_2 through the function of r_η. Note that the c_6 and c_7 terms are essentially linear terms. There is an argument against the use of the c_3 term since it violates realizability in solid-body rotation (Reynolds, 1984). The coefficient c_3 was thus designed to vanish in solid-body rotation corresponding to the absence of $\tilde{S}$ in the case (see Table 1).

The values of A_2 are obtained by solving its transport equation rather than by processing the calculated Reynolds stresses since the former approach makes solutions more stable (Craft et al., 1997). Thus, the k–ε–A_2 model needs to solve the k, $\tilde{\varepsilon}$ and A_2 transport equations. The exact A_2 equation may be written as

$$\begin{aligned}\frac{\mathrm{D}A_2}{\mathrm{D}t} = {} & \frac{1}{k}(2a_{ij}\mathscr{D}_{ij} - A_2\mathscr{D}_{kk} + 2a_{ij}P_{ij} - A_2P_{kk} + 2a_{ij}\phi_{ij} \\ & - 2a_{ij}\varepsilon_{ij} + A_2\varepsilon_{kk}),\end{aligned} \tag{3}$$

where $\mathscr{D}_{ij}, P_{ij}, \phi_{ij}$ and ε_{ij} are the diffusive transport, shear production, pressure-strain correlation and dissipation terms of $\overline{u_i u_j}$, respectively. In order to obtain $\mathscr{D}_{ij}, \phi_{ij}$ and ε_{ij}, the recent second moment modelling of UMIST is employed while P_{ij} does not need modelling. The zero gradient condition is used for the wall boundary condition of A_2. The model equations are summarized in Appendix A. Note that the A_2 equation sometimes returns unrealizable values even though a realizable second moment model is used to close the A_2 equation. This is simply because the nonlinear EVM is not fully realizable. Although Suga (1995) confirmed its realizability in fundamental strain fields, the unconditional realizability condition was not discussed due to the complexity of algebra. Hence, unrealizable values of A_2 are merely clipped during the computations as $A_2 = \min\{8/3, \max(A_2, 0)\}$.

In the $\tilde{\varepsilon}$ equation, an extra source term S_ε was added to reduce excessive length scales produced by the usual $\tilde{\varepsilon}$ (or ε) equation in stagnation regions. A slight modification has been made to S_ε after the examination of preliminary results. Since it has been found that the original term damps turbulence too much under acceleration, the term currently used is:

$$\begin{aligned}S_\varepsilon = {} & \frac{\tilde{\varepsilon} - \varepsilon}{k}\tilde{\varepsilon}\exp(-\tilde{R}_t^{\,2}/4) \\ & + \max\left\{0, -c_{\varepsilon 5}\left(\frac{\partial U_l}{\partial x_m}\frac{\partial l}{\partial x_l}\frac{\partial l}{\partial x_m}\right)\left|\frac{\partial U_p}{\partial x_q}\frac{\partial l}{\partial x_p}\frac{\partial l}{\partial x_q}\right|\right\}\frac{k(\varepsilon - \tilde{\varepsilon})}{\varepsilon},\end{aligned} \tag{4}$$

which still keeps the effect on impinging (decelerating) flows.

3. Numerical scheme

The transport equations are discretized on unstructured median dual control volumes using the third-order MUSCL-type scheme (van Albada et al., 1991) for the convection terms. The collocated grid storage arrangement is used and thus all variables are defined at the node points. For incompressible flow computations, SIMPLE (Patankar, 1980) or PISO (Issa, 1985) pressure correction algorithm is used while an implicit scheme (Nagaoka and Löhner, 1997) is used for compressible flows. One of the attractive points of the unstructured grid method is its applicability to tetrahedral cell configurations. However, in boundary layers, prismatic or hexahedral cells are desirable to reduce total cell numbers. In order to joint the

Table 1
The empirical coefficients in the cubic EVM

c_1	c_2	c_3	c_4	c_5	c_6	c_7
$-0.05f_q/f_\mu$	$0.11f_q/f_\mu$	$0.42f_q\dfrac{\tilde{S}}{f_\mu(\tilde{S}+\tilde{\Omega})}$	$-0.8f_c$	0	$-0.5f_c$	$0.5f_c$
c_μ		f_μ			η	
$f_\mu\dfrac{0.667r_\eta\left[1-\exp\left\{-0.415\exp\left(1.3\eta^{5/6}\right)\right\}\right]}{1+1.8\eta}$		$\dfrac{1.1\sqrt{\tilde{\varepsilon}/\varepsilon}\left\{1-0.8\exp(-\widetilde{R}_t/30)\right\}}{1+0.6A_2+0.2A_2^{3.5}}$			$\max(\tilde{S},\tilde{\Omega})r_\eta$	
f_q	f_c	r_η				
$\dfrac{r_\eta}{(1+0.0086\eta^2)^{1/2}}$	$\dfrac{r_\eta^2}{1+0.45\eta^{2.5}}$	$1+\left\{1-\exp\left(-8A_2^3\right)\right\}\left[1+4\sqrt{\exp\left(-\dfrac{\widetilde{R}_t}{20}\right)}\right]$				

hexahedral and the tetrahedral cells, pyramidal cells are required. Hence, the present numerical scheme is developed to treat a mixture of tetrahedral, pyramidal, prismatic and hexahedral cells so that it is very flexible to calculate complicated 3-D fields.

3.1. Integration over a cell-vertex median dual

As Fig. 1 illustrates, a cell-vertex median dual is a polyhedral control volume constructed around a node point by connecting the mid-points of the edges, the centroids of the cells sharing the edges, and the face-centroids shared by the cells. This median dual control volume leads to less grid dependency than a cell centred control volume since it is formed by more surfaces where flux is evaluated. In its nature, the surface integral by the divergence theory gives correct first-order differentiations for linearly distributed variables over tetrahedral cells (the piecewise linear approximation) while the piecewise constant approximation used by the cell centred control volume method does not. With the edge-based data structure, the first-order differentiation of a variable ϕ over a median dual is given as:

$$\left(\overline{\frac{\partial\phi}{\partial x_j}}\right)_I=\frac{1}{\mathrm{vol}_I}\sum_K\frac{1}{2}(\phi_I+\phi_J)S_K^{x_j}, \tag{5}$$

where K corresponds to the edge I–J and $\overrightarrow{S_K}:(S_K^x,S_K^y,S_K^z)$ is the normal surface-vector of the facet crossing the edge K. The second derivative for the diffusion terms of the transport equations is calculated as:

$$\left(\overline{\frac{\partial}{\partial x_j}\left(\Gamma\frac{\partial\phi}{\partial x_i}\right)}\right)_I=\frac{1}{\mathrm{vol}_I}\sum_K\frac{\Gamma_I+\Gamma_J}{2}\left.\frac{\partial\phi}{\partial x_i}\right|_K S_K^{x_j}, \tag{6}$$

where $\partial\phi/\partial x_i|_K$ is obtained by defining the local coordinate system: (ξ,η,ζ) as

$$\left.\frac{\partial\phi}{\partial x_i}\right|_K=\frac{\partial\phi}{\partial\xi}\frac{\partial\xi}{\partial x_i}+\frac{\partial\phi}{\partial\eta}\frac{\partial\eta}{\partial x_i}+\frac{\partial\phi}{\partial\zeta}\frac{\partial\zeta}{\partial x_i}. \tag{7}$$

The axes ξ, η and ζ, respectively, correspond to the I–J direction and normal directions to the vector $\overrightarrow{S_K}$. The usual central difference is applied between the points I and J for the gradient in the ξ direction while the averaged value given by Eq. (5) is employed in the η and ζ directions. Hence

$$\begin{aligned}\frac{\partial\phi}{\partial\xi}&=\phi_J-\phi_I,\\ \frac{\partial\phi}{\partial\eta}&=\overline{\phi}_x\frac{\partial x}{\partial\eta}+\overline{\phi}_y\frac{\partial y}{\partial\eta}+\overline{\phi}_z\frac{\partial z}{\partial\eta},\\ \frac{\partial\phi}{\partial\zeta}&=\overline{\phi}_x\frac{\partial x}{\partial\zeta}+\overline{\phi}_y\frac{\partial y}{\partial\zeta}+\overline{\phi}_z\frac{\partial z}{\partial\zeta},\end{aligned} \tag{8}$$

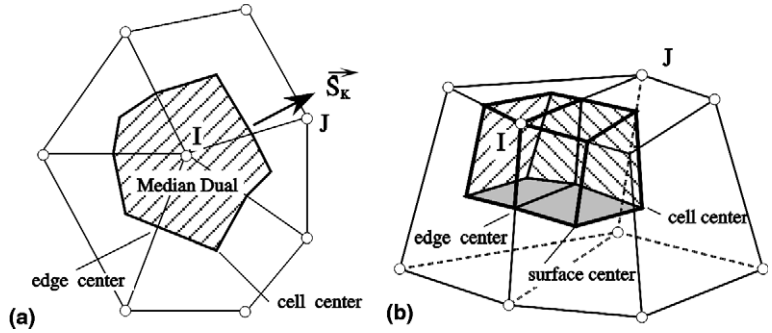

Fig. 1. Median dual control volumes: (a) 2-D; (b) 3-D (partial view).

where

$$\overline{\phi_{x_i}} = \left\{ \left(\overline{\frac{\partial \phi}{\partial x_i}} \right)_I + \left(\overline{\frac{\partial \phi}{\partial x_i}} \right)_J \right\} \Big/ 2.$$

By applying the above relations and the chain rule of the metrics:

$$\frac{\partial x_i}{\partial \xi}\frac{\partial \xi}{\partial x_j} + \frac{\partial x_i}{\partial \eta}\frac{\partial \eta}{\partial x_j} + \frac{\partial x_i}{\partial \zeta}\frac{\partial \zeta}{\partial x_j} = \delta_{ij},$$

Eq. (7) may be rewritten as

$$\left.\frac{\partial \phi}{\partial x_i}\right|_K = \frac{\partial \phi}{\partial \xi}\frac{\partial \xi}{\partial x_i} + \overline{\phi_{x_i}} - \left(\overline{\phi_{x_j}} \cdot \frac{\partial x_j}{\partial \xi} \right) \frac{\partial \xi}{\partial x_i}. \tag{9}$$

After a moderate amount of algebra, the gradient vector $\partial\xi/\partial x_i$ is expressed as

$$\frac{\partial \xi}{\partial x_i} = S_K^{x_i} \Big/ \left(S_K^x \frac{\partial x}{\partial \xi} + S_K^y \frac{\partial y}{\partial \xi} + S_K^z \frac{\partial z}{\partial \xi} \right). \tag{10}$$

Therefore, the first- and second-order differentiations can be processed by the edge-based ordering.

Although obtaining reasonable accuracy for the integration of tetrahedral cells in boundary layers is not always straightforward, the present scheme gives comparable accuracy to that of hexahedral cells. The comparison between those two meshes is made in a square sectioned turbulent duct flow as shown in Fig. 2. Both the meshes consist of $10 \times 81 \times 41$ node points distributed nonuniformly. As shown in Fig. 2(c), the mean velocity distributions by the two meshes are almost identical and thus the present scheme is confirmed to have comparable accuracy for both the mesh configurations. Note that the turbulence model used is the k–ε–A_2 model.

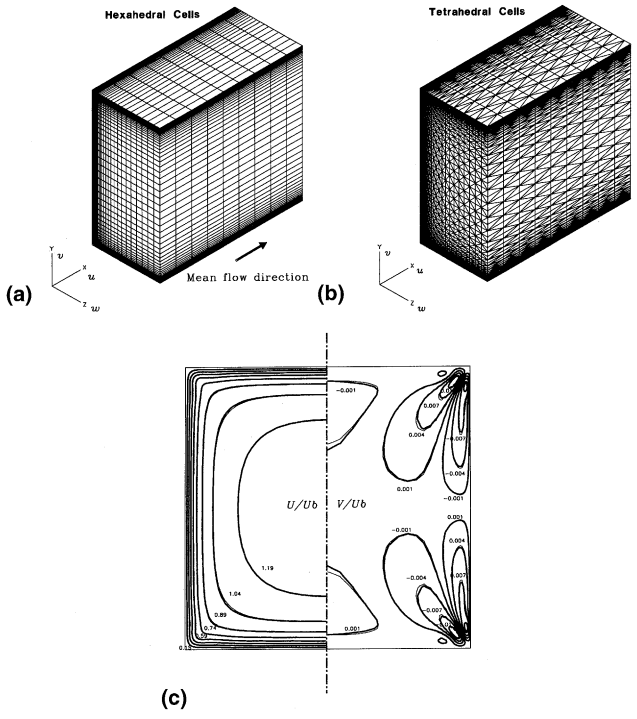

Fig. 2. Comparison of computational grids and results of hexahedral and tetrahedral meshes in a square-sectioned duct flow: ———: hexamesh; ———: tetramesh.

3.2. Numerical treatments for a nonlinear EVM

In order to stabilize the numerical solutions, the following treatments are employed in connection with the nonlinear EVM. The momentum equation with the nonlinear EVM may be written as:

$$\frac{\mathscr{D}\rho U_i}{\mathscr{D}t} = \frac{\partial}{\partial x_i}\left\{ (\mu + \mu_t)\frac{\partial U_i}{\partial x_i} \right\} - \frac{\partial (P + \frac{2}{3}\rho k)}{\partial x_i} - \frac{\partial \rho \mathrm{Hot}_{ij}}{\partial x_j}. \tag{11}$$

Some nonlinear terms can be split into two parts: $(\partial/\partial x_j)\big(\Gamma(\partial U_i/\partial x_j)\big)$ and the remainder. If the term under consideration contributes to a favourable conditioning of the linear system (typically in the case that Γ is positive), as the standard diffusion operator, it is then treated implicitly, and if not, then explicitly.

In the pressure correction for incompressible flows, the interpolation of Rhie and Chow (1983) is applied to avoid an oscillative solution caused by the collocated grid arrangement. The component $-(\partial \rho \mathrm{Hot}_{ii}/\partial x_i)$ of the third term on the rhs of Eq. (11) needs to be treated by the same manner as the pressure gradient, otherwise it also leads to pressure oscillation.

4. Applications

Since all present computations are performed by low Reynolds number turbulence models, the first node points from walls of the computational grids are carefully allocated under unity of the wall unit or an equivalent distance.

The initial condition for the values of A_2 is obtained by processing the initial stress field by its mathematical definition. For the initial guess of the strain and turbulence fields, results (which are not necessarily fully converged) of the linear k–ε EVM of Launder and Sharma (1974) (LS model hereafter) are used.

The total CPU time required for the convergence of a steady-state computation by the k–ε–A_2 model is approximately twice as long as that of the LS model though it varies in the cases. Note that every present test flow case is in a steady-state condition.

4.1. U-bend flows

As shown in Fig. 3, the square sectioned 180° U-bend duct flows of two curvature ratios: $Rc/D = 3.357$ and 0.65 (Chang

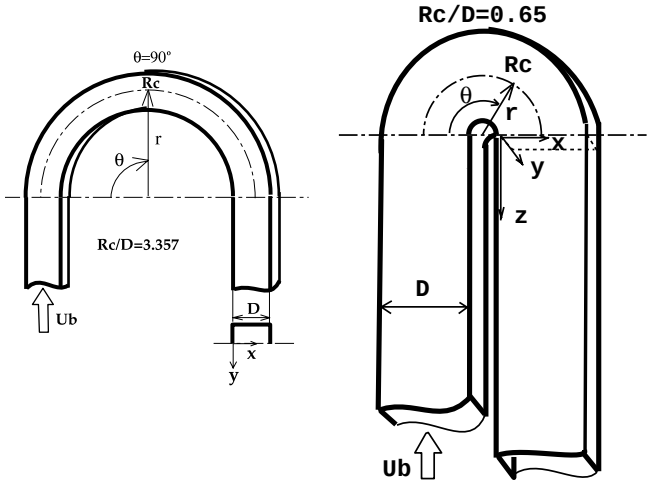

Fig. 3. Square-sectioned 180° U-bend duct flows.

et al., 1983; Cheah et al., 1994) are considered. In the case of $Rc/D = 3.357$, no separation occurs whilst in the strong curvature case of $Rc/D = 0.65$, a separating flow appears along the suction side. The computational grids cover up to the symmetry plane and, respectively, consist of 121 (streamwise) $\times 81(x) \times 41(y)$ (with 1D inlet, 3D outlet tangents) and $151 \times 100 \times 50$ (with 3D inlet, 9D outlet tangents) nodes which have been well calibrated for grid-independent computations. (Several preliminary runs have been performed to confirm the grid-independency.) For providing the inlet flow conditions, separate computations of fully developed straight duct flows have been performed.

In order to examine the prepared inlet condition, Fig. 4 compares the predictions with the experiments of the fully developed square sectioned straight duct by Cheesewright et al. (1990). Although the velocity component W causing the secondary flow is underpredicted at some sections (Fig. 4(b)), the streamwise velocity U (Fig. 4(a)) and the rms normal stress components (Fig. 4(c)) are generally well predicted by the k–ε–A_2 model. With the linear k–ε EVM (Launder and Sharma, 1974), one cannot obtain the W component nor the stress anisotropy. Hence, the fully developed inlet conditions imposed on the U-bend flows are considered to be reasonable. (The nonlinear stress–strain relation may need to be retuned for a better secondary flow prediction if necessary.)

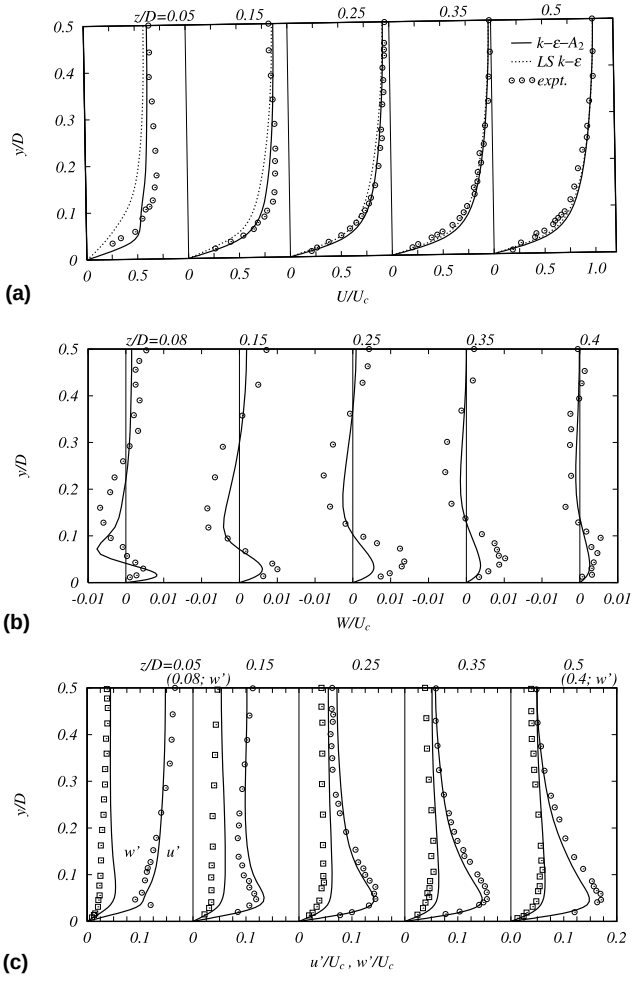

Fig. 4. Square-sectioned straight duct flow at $Re = 5000$; experiments: Cheesewright et al. (1990).

Fig. 5 shows the comparisons between the predictions and the experiments of the U-bend flow of $Rc/D = 3.357$ at $Re = 56\,700$. Fig. 5(a) compares the streamwise mean velocity distributions at the four sections of $\theta = 45°$, 90°, 130° and 177° in the symmetry plane ($2y/D = 0$). Figs. 5(b)–(d) compare the distributions of the streamwise mean velocity and the rms normal stresses at $\theta = 90°$, respectively. Clearly, the k–ε–A_2 model gives far better results than the linear EVM. Particularly, the k–ε–A_2 model successfully reproduces the "camel back" profiles of the streamwise velocity distributions appearing at the sections of $\theta = 90°$ and 130°. The prediction quality is clearly better than the traditional ASM approaches reviewed by Iacovides and Launder (1995).

As shown in Fig. 6, the reasonable accuracy of the k–ε–A_2 model is also confirmed in the strong curvature case of $Rc/D = 0.65$ at $Re = 100\,000$. The recirculating region and recovery from it in the downstream region is reasonably well predicted compared with the LS model. Obviously, the linear model predicts a too weak but long recirculation. Although the agreement is not perfect, the level of the predicted rms normal stress of the k–ε–A_2 model is generally better than the LS model's.

Overall, it can be said that the k–ε–A_2 model has reasonable sensitivity to the curvature of 3-D duct flows. This is a preferable feature for predicting IC engine port flows which is the topic of the following subsection.

4.2. IC engine port-cylinder flows

Fig. 7 illustrates the typical computational grid for the half model of the IC engine port-cylinder flows. The presently used grids have 370 000–400 000 hexahedral cells. A finer grid consisting of twice node points has been also used though the predicted discharge coefficient C_f changes only 2%. The definition of the discharge coefficient is

$$C_f = \frac{\dot{m}}{\pi D_{valve} L_{lift}} \left\{ 2P_0\rho_0 \frac{\gamma}{\gamma - 1} \left(\frac{P_{exit}}{P_0} \right)^{2/\gamma} \times \left[1 - \left(\frac{P_{exit}}{P_0} \right)^{(\gamma-1)/\gamma} \right] \right\}^{-1/2}, \quad (12)$$

where $\dot{m}, D_{valve}$ and L_{lift} are, respectively, the mass flow rate, the valve diameter and the valve-lift distance. The port and cylinder diameters are, respectively, 23 and 75 mm, and the valve diameter D_{valve} and the valve-lift distance L_{lift} are 28 and 7 mm, respectively. A prescribed pressure difference $\Delta P = 2.67$ kPa and a total pressure $P_0 = 100.4$ kPa with the stagnation temperature 299 K and density $\rho_0 = 1.17$ kg/m^3 are used. A uniform inlet flow with 5% turbulence is imposed on the present compressible flow computations. The inlet condition of the turbulent dissipation rate is obtained through the assumption of the inlet turbulent length-scale as 50% of the port diameter D. The Reynolds number based on the inlet flow and the port diameter is 91 000.

Fig. 8 shows the predicted discharge coefficient C_f against R/D compared with the experiments by Kawazoe (1993). The predicted behaviour by the k–ε–A_2 model is reasonably acceptable while the LS model lacks reliability. The discharge rate is considered to be significantly affected by the wall friction and the separation bubble appearing along the suction side of the port. Since the k–ε–A_2 model predicts the U-bend flows with satisfactory sensitivity to the curvature ratio, its success is reasonably expected. Also, in the region between the valve and the valve-seat where the flow is strongly accelerated, the linear EVM tends to predict too excessive turbulence which increases the wall friction whilst the k–ε–A_2 model does not.

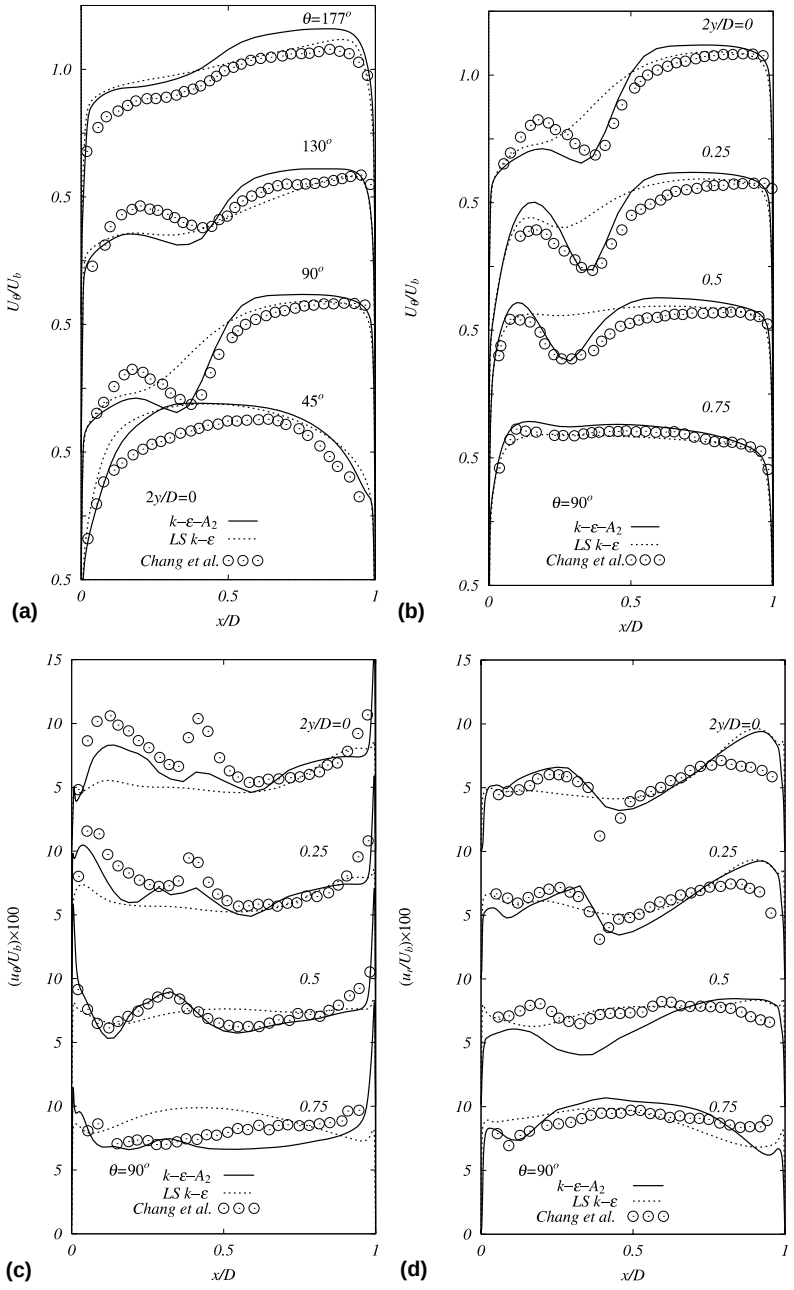

Fig. 5. U-bend duct flow of $Rc/D = 3.357$ at $Re = 56\,700$.

Fig. 9 compares the velocity vectors at four sections in the symmetry plane of the two cases of $R/D = 1$ and 2. Evidently, the mean flow patterns in the cylinders are found to be captured better by the k–ε–A_2 model though perfect agreement cannot be found in such complex flow fields.

4.3. Aerodynamic bluff body flows

Fig. 10 illustrates a typical computational grid used in the present study for incompressible flows around the aerodynamic bluff bodies of Maeda et al. (1990) which is set $0.227H$ above a floor (H: bluff body height). The grids for half models of five base angle cases ($\theta = 25°$, 35°, 40°, 45°, and 55°) have 311 000–467 333 cells composed of all hexahedral or a mixture of prismatic and hexahedral cells. (A finer grid consisting of roughly twice cells has produced the drag coefficient 2% lower.) The length and width of the bluff body are $(2 + 1/\tan\theta)H$ and $1.4H$, respectively. The inlet uniform flow with 2% free stream turbulence is imposed $5H$ upstream of the leading edge while out-flow conditions are set about at $20H$ downstream of the trailing edge. Setting the inlet turbulent dissipation rate is made by assuming that the inlet turbulent length-scale is 10% of the hydraulic diameter of the inlet. The free stream boundary is set at $6.3H$ above the floor and spanwise symmetry conditions are also imposed at $4.3H$ away from the symmetry plane. The bulk Reynolds number based on H is 4.4×10^5.

Fig. 11 compares predicted distributions of the vorticity ω_z in the three typical cases by the k–ε–A_2 model. Clearly, apparent vortex patterns can bee seen. At $\theta = 25°$, there is al-

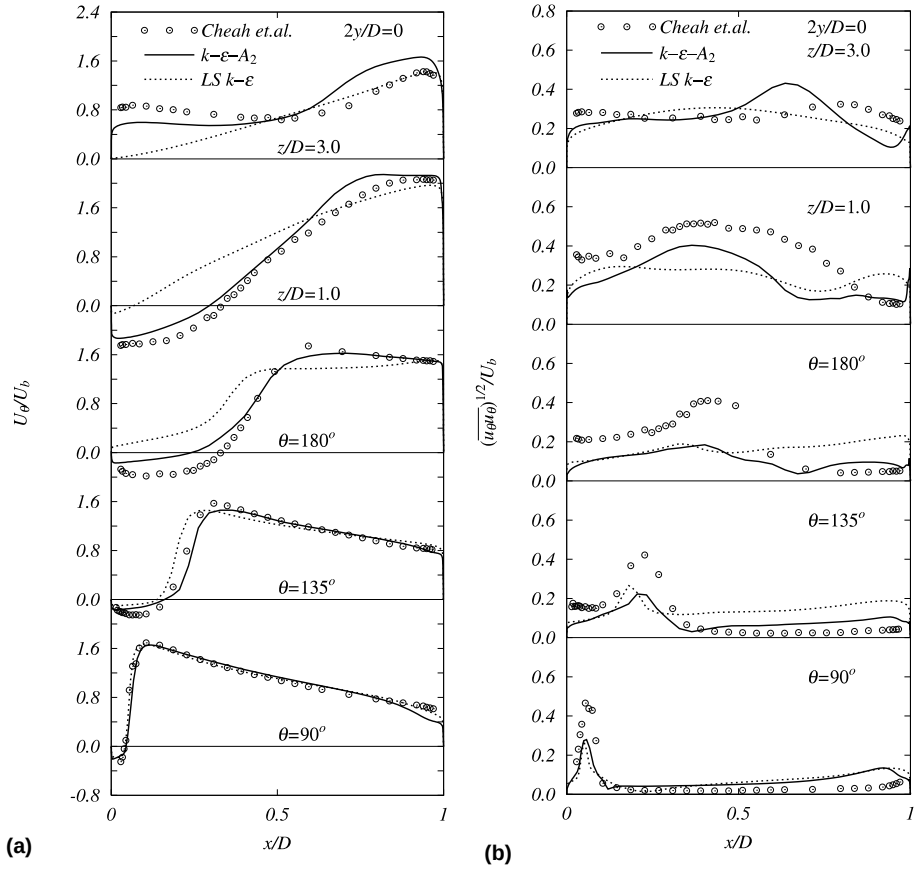

Fig. 6. U-bend duct flow of $Rc/D = 0.65$ at $Re = 10^5$.

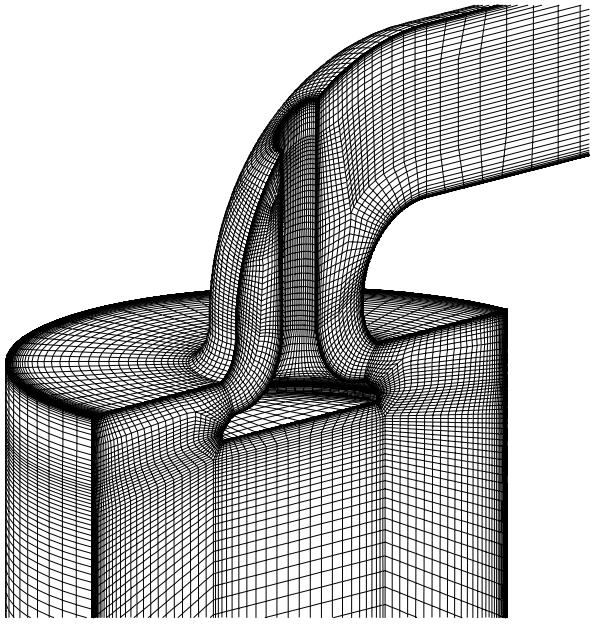

Fig. 7. Computational grid for IC engine port-cylinder flow.

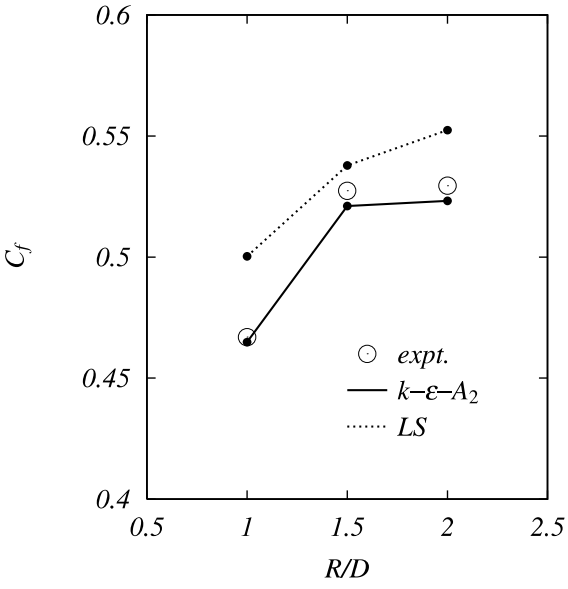

Fig. 8. Discharge coefficient at $Re = 91000$.

most no separation bubble along the slant base (while the k–ε–A_2 model predicts a tiny separation bubble). According to the increase of the angle toward a *critical* point, (which is about 40° suggested by the experiments), a separation bubble appears and grows ($\theta = 35°$). Then, the separation bubble becomes unstable and eventually bursts when the angle exceeds the critical point ($\theta = 55°$). According to the burst of the separation bubble, the drag coefficient C_D ($= 2F_D/$

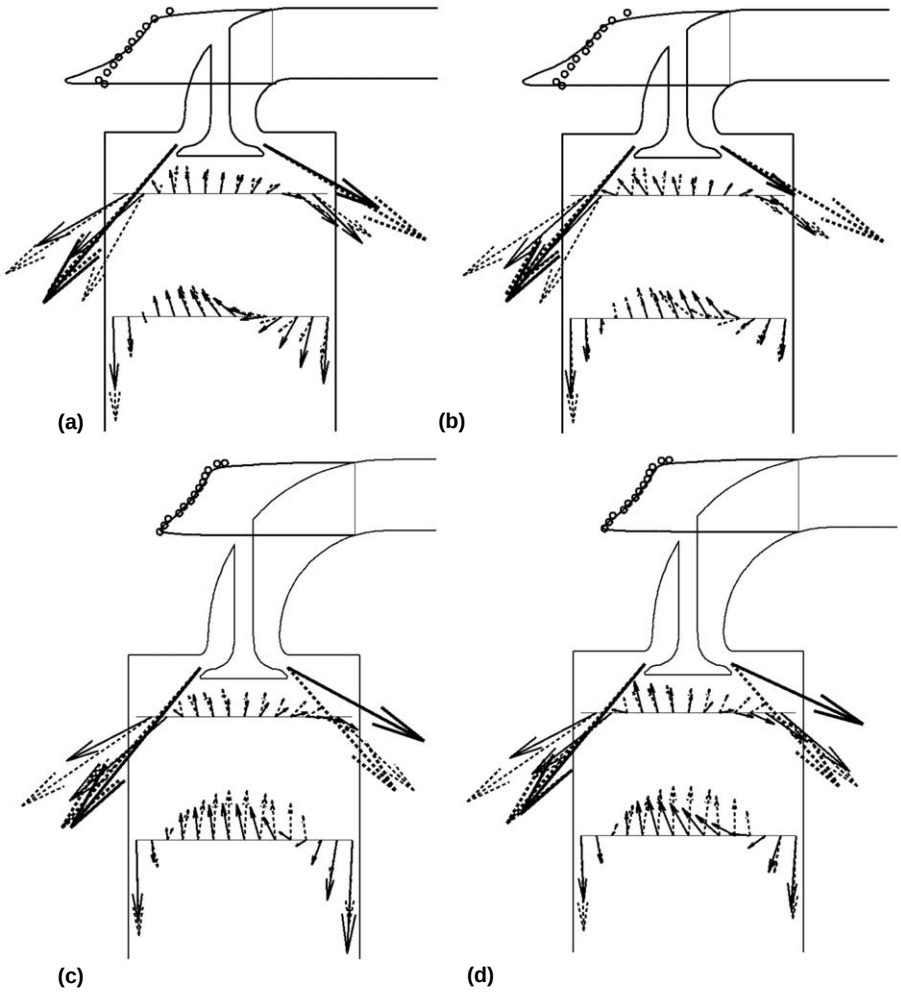

Fig. 9. Vector plots in the symmetry plane: ———: prediction; – – – – – – –, ○ ○ ○: Kawazoe (1993): (a) k–ε–A_2 at $R/D = 1$; (b) LS at $R/D = 1$; (c) k–ε–A_2 at $R/D = 2$; (d) LS at $R/D = 2$.

($\rho U_b^2 A$), F_D: drag; A: cross-sectional area) reduces drastically as shown in Fig. 12.

Fig. 13 compares distributions of the pressure coefficient. The k–ε–A_2 model performs generally well in the lower slant angle case of $\theta = 25°$ though its prediction just behind the upstream edge of the slant base is slightly lower than the experiments. This is due to a small separation bubble predicted while the experiments suggests that there is almost no separation. In the cases of $\theta = 35°$ and 55°, however, Figs. 13(b) and (c) suggest that the predictions along the slant base should be lower. Consequently, as shown in Fig. 12, the predicted drag coefficient becomes higher at $\theta = 25°$ but lower at $\theta = 35°$ and 55° than the experiments though the model performance is reasonably acceptable. The linear model generates too excessive turbulence which produces high friction around the leading edge and thus its predicted drag coefficient is always significantly higher.

Although the k–ε–A_2 model is reasonably useful for evaluating the drag performance, some more discussions are obviously needed for separating wake flows. Due to the limited measurements around the bluff bodies, a further discussion is hard to be made, unfortunately. Thus, in the following subsection, a cubical obstacle flow is considered for the detailed discussion on the model performance in a separating wake flow region.

4.4. Cubical obstacle flow

Fig. 14 zooms up the computational grid which consists of 813856 unstructured hexahedral cells for the flow around a cubical obstacle mounted in a channel. This test case is from the study of Martinuzzi et al. (1993) and was also selected for a test case of the sixth ERCOFTAC/IAHR/COST Workshop on Refined Flow Modelling held at TU Delft, 1997. The Reynolds number based on the bulk velocity and the cube height H is 80 000. The computational region has $14H$ streamwise, $2H$ cross-streamwise and $4.5H$ spanwise (from the symmetry plane) lengths and the cube is mounted on the bottom wall $3H$ downstream from the inlet. The coarser grid consisting of half node points has been also tested. The difference between the predicted reattachment lengths is 3%, and thus the finer grid is used for the present discussion. To provide the inlet condition, a separate computation for a fully developed channel flow has been performed.

Fig. 15 compares the predicted streamwise mean velocity distributions of the k–ε–A_2 and the LS models. As shown in Fig. 15(a), the flow separates but does not reattach on the top face of the cube. The result of the k–ε–A_2 model also does not show a reattachment while its recirculating region is thicker at $x/H = 1$ even though the negative velocity at $x/H = 0.5$ is rather weaker. The LS model predicts smaller separation and

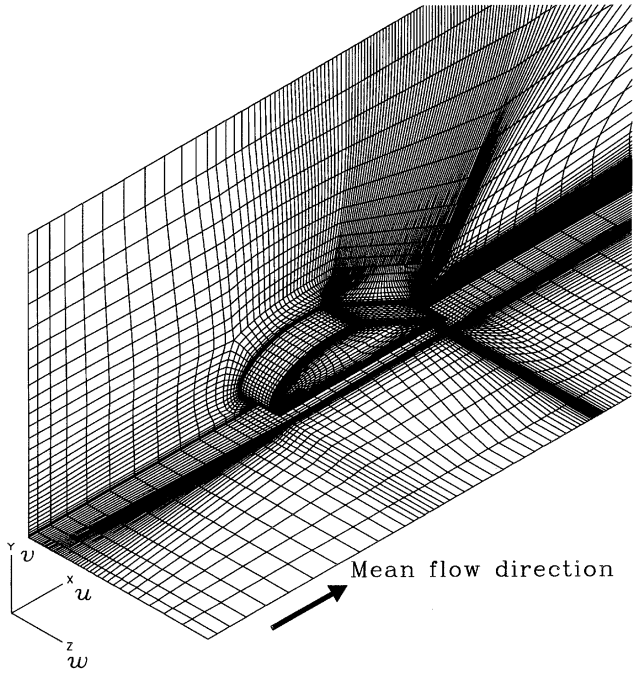

Fig. 10. Computational grid around an aerodynamic bluff body.

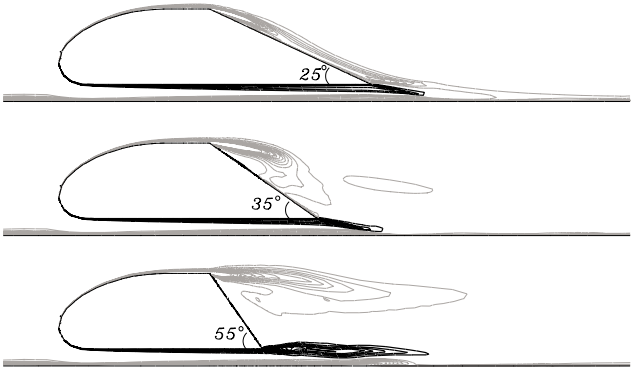

Fig. 11. Vorticity ω_z contour lines predicted by the k–ε–A_2 model: black lines: positive values; grey lines: negative values.

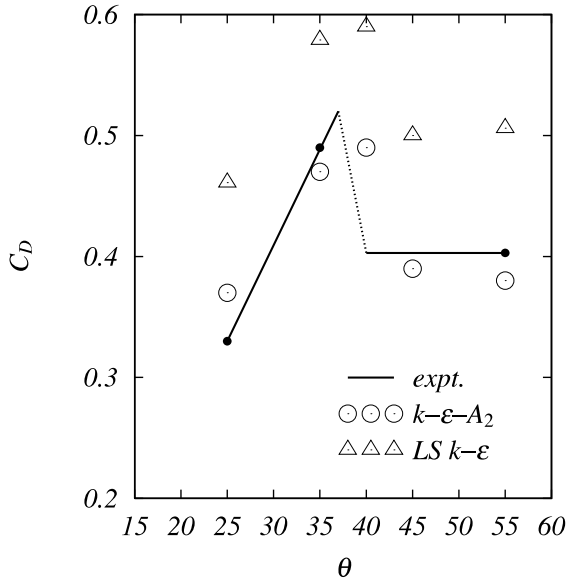

Fig. 12. Drag coefficient.

the flow reattaches on the top face. In front of the cube, as in Fig. 15(b), the k–ε–A_2 predicts too strong reverse flow though the LS model does not. This implies that the additional source term for impinging flows: Eq. (4), of the dissipation equation is too strong in this flow case. (Note that any additional term for correcting excessive length-scales is not used in the presently discussed LS model.) Behind the cube, clearly, both the models predict too long recirculating flow compared with the experiments. As Fig. 16 illustrates, the reattachment length of the k–ε–A_2 is nearly two times as long as that suggested by the experiments, which is about $2.7H$.

The k–ε–A_2 model also tends to predict longer reattachment lengths in some 2-D flow fields though they are not always so bad as in this 3-D case. As shown in Fig. 17, the predicted profiles of the back-step flow are reasonable though the predicted reattachment length is 6% longer than the experimental value of $6.5H$. (The LS model predicts 6% shorter.) In the case of the 2-D square obstacle flow of Dimaczek et al. (1989), the predicted reattachment length by the k–ε–A_2 model is $10H$ while the experimental one is $8.1H$ at $Re = 40000$. (The LS model predicts it as $7.8H$.)

In the 3-D case, the recirculating region becomes significantly shorter than the 2-D case due to the interaction with typical 3-D phenomena such as a horseshoe vortex around an obstacle. This may make the prediction difficult. In fact, all of the moment closures including recent full second moment closures tested in the ERCOFTAC/IAHR workshop showed similar tendencies which were rather poor (Rautaheimo and Siikonen, 1997). (Ironically, amongst the tested models, the standard k–ε model with wall functions showed the best performance.)

Obviously, improvements in the modelling for 3-D separation are strongly required. Note that the k–ε–A_2 model does not necessarily perform badly in separating flows, since as discussed in Section 4.1, it shows reasonable performance in the confined separating flow. Besides, a transient computational method (Kenjereš and Hanjalić, 1999) with phase averaging is also worth considering. Some unsteady effect may need to be accounted even in computations for the steady-state performance since this sort of flow sheds vortices periodically.

5. Concluding remarks

This paper has discussed on the numerical aspects and the 3-D application results of the k–ε–A_2 three-equation cubic nonlinear EVM. The following remarks summarizes the present work.

1. A numerical scheme for complicated turbulent flows by the collocated cell-vertex unstructured grid method is developed. This scheme treats a mixture of tetrahedral, pyramidal, prismatic and hexahedral cells by the edge-based data structure. The numerical accuracy is confirmed to be almost identical in different cell configurations.
2. The required total CPU time for convergence by the k–ε–A_2 model is approximately twice as long as that of the linear EVM in the present 3-D flow computations. This is acceptable for practical applications.

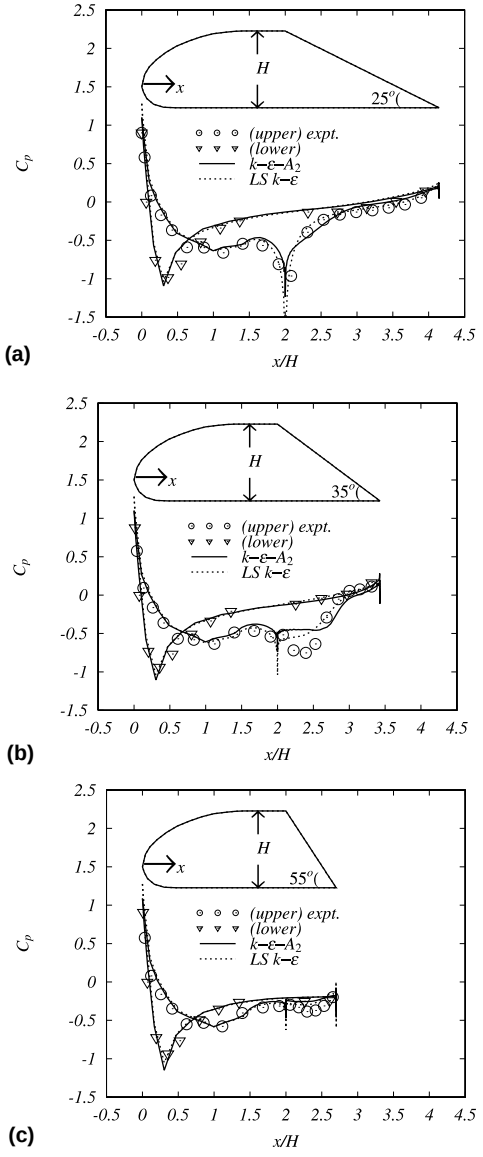

Fig. 13. Pressure coefficient distributions in the symmetry plane: experiments: Maeda et al. (1990).

3. Fairly satisfactory results are obtained by the k–ε–A_2 model in the square sectioned U-bend duct flows. The results are comparable to those of a second moment closure which requires far more CPU resources.
4. Due to the reasonable sensitivity to the curvature, the performance of the k–ε–A_2 model for the IC engine port-cylinder flows is adequately satisfactory.
5. The k–ε–A_2 model predicts drag coefficients of bluff bodies far better than the linear EVM though its prediction accuracy for the pressure coefficients is unsatisfactory when the flow separates along the slant base.
6. The poor performance shown in the 3-D separating wake flow suggests that improvements in predicting 3-D separation with a horseshoe vortex are strongly required.

Acknowledgements

We owe a debt of gratitude to Dr. H. Iacovides of UMIST for his kindly providing the experimental database of the U-bend duct flow. We also thank Dr. H.-Y. Li of CFD Research Corp. for her advice on computing U-bend duct flows.

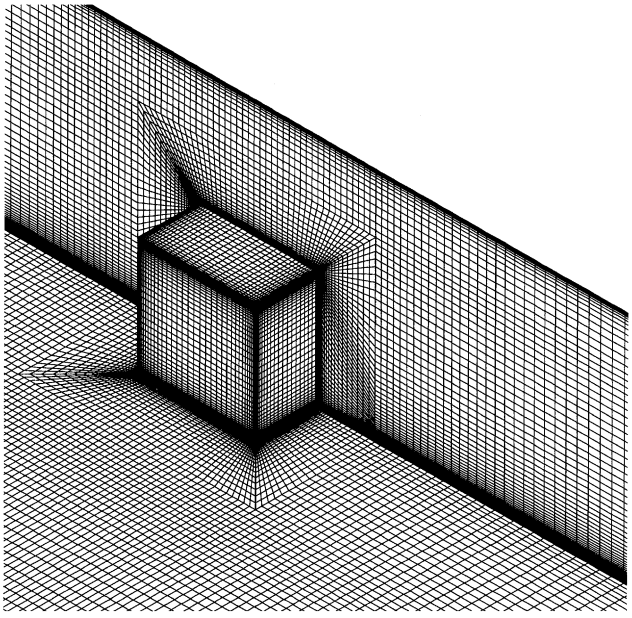

Fig. 14. Computational grid around a cube.

Appendix A. The k–ε–A_2 model equations

The k–ε–A_2 model equations proposed by Craft et al. (1997) may be summarized in the forms as below.

The transport equation for k is:

$$\frac{\mathrm{D}k}{\mathrm{D}t} = \frac{\partial}{\partial x_k}\left\{\left(\nu\delta_{kl} + 0.22 f_g \overline{u_k u_l}\frac{k}{\tilde{\varepsilon}}\right)\frac{\partial k}{\partial x_l}\right\} + P_k - \varepsilon, \tag{A.1}$$

where

$$f_g = \{5(\varepsilon/\tilde{\varepsilon})^{1/2} - 4(\varepsilon/\tilde{\varepsilon})^{1/4}\} \quad \text{and} \quad P_k = P_{kk}/2;$$

$$P_{ij} = -\left(\overline{u_i u_k}\frac{\partial U_j}{\partial x_k} + \overline{u_j u_k}\frac{\partial U_i}{\partial x_k}\right).$$

The transport equation for $\tilde{\varepsilon}$ is:

$$\frac{\mathrm{D}\tilde{\varepsilon}}{\mathrm{D}t} = \frac{\partial}{\partial x_k}\left\{\left(\nu\delta_{kl} + 0.18 f_g \overline{u_k u_l}\frac{k}{\tilde{\varepsilon}}\right)\frac{\partial \tilde{\varepsilon}}{\partial x_l}\right\} + c_{\varepsilon 1} P_k \frac{\tilde{\varepsilon}}{k} - c_{\varepsilon 2}\frac{\tilde{\varepsilon}^2}{k} + P_{\varepsilon 3} + S_\varepsilon, \tag{A.2}$$

where

$$c_{\varepsilon 1} = 1 + 0.15\left(1 - A^*\right),$$

$$c_{\varepsilon 2} = \frac{1.92}{1 + 0.7\left(1 - \left(1 + \widetilde{R}_t{}^2/400\right)^{-1}\right)\sqrt{A_2}\max(0.25, A^*)}$$

and

$$P_{\varepsilon 3} = 1.2\nu\nu_t \frac{\partial^2 U_i}{\partial x_k \partial x_j}\frac{\partial^2 U_i}{\partial x_k \partial x_j} + \nu\frac{\nu_t}{k}\frac{\partial k}{\partial x_k}\frac{\partial U_i}{\partial x_l}\frac{\partial^2 U_i}{\partial x_k \partial x_l}.$$

The additional term S_ε is given by Eq. (4).

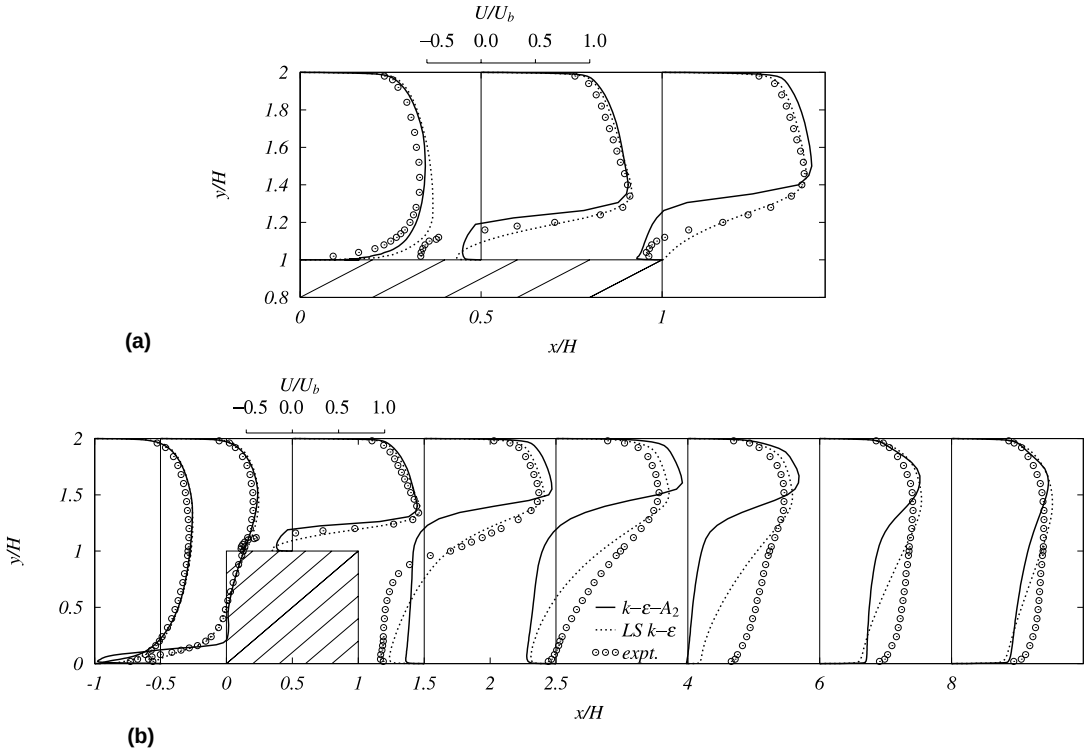

Fig. 15. Mean velocity distribution in the symmetry plane at $Re = 8 \times 10^4$.

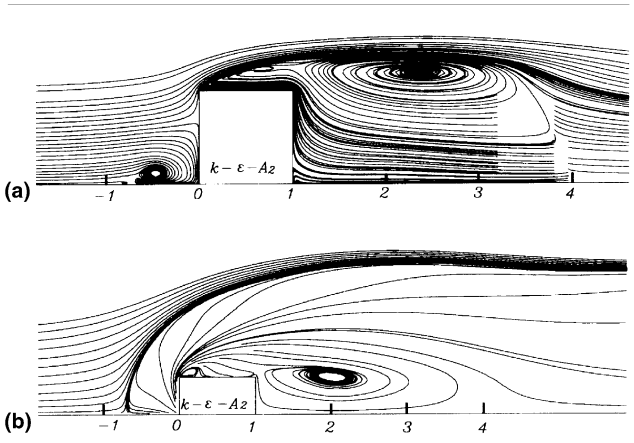

Fig. 16. Streamlines of the mean flow projected onto the symmetry plane (a), and the floor (b).

The modelled A_2 transport equation may be written as

$$\frac{\mathrm{D}A_2}{\mathrm{D}t} = \mathscr{D}_{A_2} + P_{A_2} + \Pi_{A_2} - \varepsilon_{A_2}, \tag{A.3}$$

where $\mathscr{D}_{A_2}$, P_{A_2}, Π_{A_2} and ε_{A_2} are the terms associated with diffusion, shear production, pressure correlation and dissipation, respectively. The $\mathscr{D}_{A_2}$, is modelled as

$$\mathscr{D}_{A_2} = \frac{\partial}{\partial x_k}\left\{\left(\nu\delta_{kl} + 0.22 f_g \overline{u_k u_l}\frac{k}{\tilde{\varepsilon}}\right)\frac{\partial A_2}{\partial x_l}\right\}. \tag{A.4}$$

The source terms are expressed as

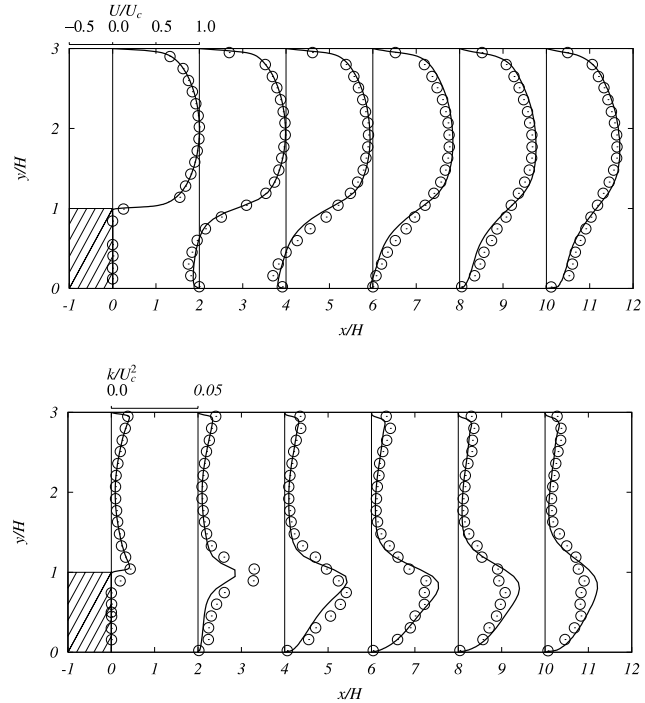

Fig. 17. Two-dimensional back step flow at $Re = 5000$: ———: k–ε–A_2; ○ ○ ○: Kasagi and Matsunaga (1995).

$$P_{A_2} + \Pi_{A_2} = -\frac{0.8}{k}\left(P_k A_2 - P_{ij} a_{ij}\right) - 6.2 \min[\sqrt{A_2}, 0.5]\sqrt{A^*} f_\phi \frac{\varepsilon}{k}(A_2 + 1.2A_3) + \phi^{\mathrm{w}}_{A_2}, \tag{A.5}$$

Table 2
The model functions of the k–ε–A_2 model

l_f	f_ϕ	f_A	f_ε	f_ε^*
$\dfrac{1-\exp(-\widetilde{R}_t/30)}{1+3.5A_2^2}\,l$	$1-\exp\left\{-\left(\dfrac{\widetilde{R}_t}{80}\right)^2\right\}$	$\exp(-20A''^2)$	$1-f_\phi\{1-\exp(-20A^{*1.5})\}$	$1-\exp\left(\dfrac{-\widetilde{R}_t}{1+2A_2^2}\right)$
A^*	A'		A''	
$f_A A' + (1-f_A)A''$	$A\left\{1-\exp\left(\dfrac{-\widetilde{R}_t{}^2}{1+24A_2}\right)\right\}$		$\left[1-\dfrac{9}{8}\left\{A_2-A_3\left(\dfrac{A_2}{a_{ij}a_{ij}}\right)^{1.5}\right\}\right]\left[1-\exp\left\{-\left(\dfrac{\widetilde{R}_t}{10}\right)^2\right\}\right]\dfrac{\tilde{\varepsilon}}{\varepsilon}$	

where the wall reflection part is

$$\phi_{A_2}^{w}=\frac{0.528A_2^2}{k}\left(\frac{\partial U_l}{\partial x_m}\overline{u_l u_m}\right)\left(a_{ij}\frac{\partial l_f}{\partial x_i}\frac{\partial l_f}{\partial x_j}\right)+0.96A_2^2\frac{\partial U_i}{\partial x_m}a_{ml}a_{ij}\frac{\partial l_f}{\partial x_l}\times\frac{\partial l_f}{\partial x_j}+2.4f_\phi A_2^2\left(\frac{\partial U_l}{\partial x_m}\frac{\partial l_f}{\partial x_l}\frac{\partial l_f}{\partial x_m}\right)\left(a_{ij}\frac{\partial l_f}{\partial x_i}\frac{\partial l_f}{\partial x_j}\right).$$

The dissipation term is

$$\varepsilon_{A_2}=\frac{2F_{\varepsilon 1}F_{\varepsilon 2}}{k}-\frac{2\varepsilon A_2}{k}\left(1-\sqrt{A^*}-F_{\varepsilon 1}\right),\tag{A.6}$$

where

$$F_{\varepsilon 1}=f_\varepsilon\Bigg/\left(1+\frac{5\nu f_\varepsilon^*}{\varepsilon}\frac{\partial\sqrt{k}}{\partial x_k}\frac{\partial\sqrt{k}}{\partial x_m}\frac{\overline{u_k u_m}}{k}\right),$$

$$F_{\varepsilon 2}=2\nu f_\varepsilon^* a_{ij}\frac{\partial\sqrt{k}}{\partial x_m}\left(\frac{\partial\sqrt{k}}{\partial x_i}\frac{\overline{u_j u_m}}{k}+\frac{\partial\sqrt{k}}{\partial x_j}\frac{\overline{u_i u_m}}{k}\right).$$

The model functions are listed in Table 2.

References

Abe, K., Kondoh, T., Nagano, Y., 1997. On Reynolds-stress expressions and near-wall scaling parameters for predicting wall and homogeneous turbulent shear flows. Int. J. Heat Fluid Flow 18, 266–282.

Ahmed, S.R., Ramm, G., Faltin, G., 1984. Some salient features of the time-averaged ground vehicle wake. SAE Tech. Paper, No. 840300.

Barakos, G., Drikakis, D., 2000. Investigation of nonlinear eddy-viscosity turbulence models in in shock/boundary-layer interaction. AIAA J. 38, 461–469.

Chang, S.M., Humphrey, J.A.C., Modavi, A., 1983. Turbulent flow in a strongly curved U-bend and downstream tangent of square cross-sections. Physico Chem. Hydrodyn. 4, 243–269.

Cheah, S.C., Iacovides, H., Jackson, D.C., Ji, H., Launder, B.E., 1994. LDA investigation of the flow development through rotating U-ducts. ASME 94-GT-226.

Cheesewright, R., McGrath, G., Petty, D.G., 1990. LDA measurements of turbulent flow in a duct of square cross section at low Reynolds number. Aero. Eng. Dept. Rep., Queen Mary Westfield College, ER 1011.

Chen, W.L., Lien, F.S., Leschziner, M.A., 1998a. Non-linear eddy viscosity modelling of transitional boundary layers pertinent to turbomachine aerodynamics. Int. J. Heat Fluid Flow 19, 297–306.

Chen, W.L., Lien, F.S., Leschziner, M.A., 1998b. Computational prediction of flow around highly loaded compressor-cascade blades with non-linear eddy viscosity models. Int. J. Heat Fluid Flow 19, 307–319.

Craft, T.J., Launder, B.E., Suga, K., 1996. Development and application of a cubic eddy-viscosity model of turbulence. Int. J. Heat Fluid Flow 17, 108–115.

Craft, T.J., Launder, B.E., Suga, K., 1997. Prediction of turbulent transitional phenomena with a nonlinear eddy-viscosity model. Int. J. Heat Fluid Flow 18, 15–28.

Dimaczek, G., Kessler, R., Martinuzzi, R., Tropea, C., 1989. The flow over two-dimensional, surface-mounted obstacles at high Reynolds numbers. In: Proceedings of the Seventh Symposium on Turbulent Shear Flows, Stanford University, pp. 10.1.1–10.1.6.

Gatski, T.B., Speziale, C.G., 1993. On explicit algebraic stress models for complex turbulent flows. J. Fluid Mech. 254, 59–78.

Iacovides, H., Launder, B.E., 1995. Computational fluid dynamics applied to internal gas-turbine blade cooling: a review. Int. J. Heat Fluid Flow 16, 454–470.

Issa, R., 1985. Solution of implicitly discretized fluid flow equations by operator splitting. J. Comput. Phys. 62, 40–65.

Kasagi, N., Matsunaga, A., 1995. Three-dimensional particle-tracking velocimetry measurement of turbulence statistics and energy budget in a backward-facing step flow. Int. J. Heat Fluid Flow 16, 477–485.

Kawazoe, H., 1993. A study on intake airflow and air–fuel mixture formulation in an internal combustion gasoline engine. Dr. Eng. thesis, Nagoya University, Japan.

Kenjereš, S., Hanjalić, K., 1999. Transient analysis of Rayleigh–Bénard convection with a RANS model. Int. J. Heat Fluid Flow 20, 329–340.

Launder, B.E., Sharma, B.I., 1974. Application of the energy-dissipation model of turbulence to the calculation of flow near a spinning disc. Lett. Heat Mass Transfer 1, 131–138.

Maeda, K., Kobayashi, N., Katsumata, S., 1990. Analysis of air flow behaviour around a vehicle to improve vehicle aerodynamic characteristic. Trans. JSAE 45, 54–59.

Martinuzzi, R., Melling, A., Tropea, C., 1993. Reynolds stress field for the turbulent flow around a surface-mounted cube placed in a channel. In: Proceedings of the Ninth Symposium on Turbulent Shear Flows, Kyoto, 13-4-1.

Myong, H.K., Kasagi, N., 1990. Prediction of anisotropy of the near wall turbulence with an anisotropic low-Reynolds number k–ε turbulence model. ASME J. Fluid Eng. 112, 521–524.

Nagaoka, M., Löhner, R., 1997. Comparisons of preconditioned iterative methods in the implicit unstructured solver of compressible flow. Trans. JSME B 63, 153–160.

Patankar, S.V., 1980. Numerical Heat Transfer and Fluid Flow. Hemisphere/McGraw Hill, Washington.

Rautaheimo, P., Siikonen, T., 1997. Case 6.3 Flow around surface-mounted cubical obstacle. In: Hanjalić, K., Obi, S. (Eds.), Proceedings of the Sixth ERCOFTAC/IAHR/COST Workshop on Refined Flow Modelling, TU Delft, The Netherlands.

Reynolds, W.C., 1984. Physical and analytical functions, concepts and new directions in turbulence modelling and simulation. In: Launder, B.E., Rodi, W., Reynolds, W.C. (Eds.), Turbulence Models and Their Applications, vol. 2, Eyrolles, Paris.

Rubinstein, R., Barton, J.M., 1990. Non-linear Reynolds stress models and renormalization group. Phys. Fluids A 2, 1472–1476.

Rhie, C.M., Chow, W.L., 1983. Numerical study of the turbulent flow past an airfoil with trailing edge separation. AIAA J. 21, 1525–1532.

Shih, T.-H., Zhu, J., Lumley, J.L., 1995. A new Reynolds stress algebraic equation model. Comput. Methods Appl. Mech. Engrg. 125, 287–302.

Suga, K., 1995. Development and application of a non-linear eddy viscosity model sensitized to stress and strain invariants. PhD thesis, UMIST, Manchester, UK.

Van Albada, G.D., van Leer, B., Roberts, W.W., 1991. A comparative study of computational methods in cosmic gas dynamics. Astron. Astrophys. 29, 1092–1110.